PCCP

ROYAL SOCIETY OF CHEMISTRY

PAPER

View Article Online
View Journal | View Issue

Cite this: *Phys. Chem. Chem. Phys.*, 2024, **26**, 3462

Hydration effects on thermal transitions and molecular mobility in Xanthan gum polysaccharides†

Sokratis N. Tegopoulos, [a] Aristeidis Papagiannopoulos [b] and Apostolos Kyritsis *[a]

In this work, the xanthan gum (XG) polysaccharide is studied over a wide range of temperatures and water fractions $0 \leq h_w \leq 0.70$ (on a wet basis) by employing differential scanning calorimetry (DSC) and broadband dielectric spectroscopy (BDS). The investigation reveals that the critical water fraction for ice formation is about 0.35. Glass transition temperature (T_g) was determined through calorimetry experiments for all the samples studied. Water acts as a strong plasticizer, *i.e.*, decreasing T_g, for water fractions up to about 0.35. A secondary (local) relaxation process is recorded in both dry and hydrated samples, which is sensitive to the presence of water molecules. This fact indicates that this process originates due to the orientation of small polar groups of the side chain, or/and due to the local main chain dynamics. Two types of long-range charge transport processes were resolved. The first is related to the conductive paths being formed *via* bulk-like ice structures (at high hydration levels), whereas the second can be attributed to proton mobility *via* the hydrogen bond (HB) network of non-freezing water existing in XG. Interestingly, this process is exactly the same in all the hydrated samples with $h_w > 0.25$. With respect to the sample with $h_w = 0.27$, a Vogel–Tammann–Fulcher (VTF)-like polarization process has also been recorded which seems to be related to long-range charge mobility *via* interconnected water clusters. As far as we are aware, this is the first time that XG is studied in terms of glass transition and molecular mobility over a wide range of hydration levels combining DSC and BDS techniques.

Received 25th September 2023,
Accepted 28th December 2023

DOI: 10.1039/d3cp04643e

rsc.li/pccp

1. Introduction

Polysaccharides are among the most important organic molecules in nature. Their primary structure exhibits great diversity in terms of composition, molecular weight, and configuration. This fact results in an almost infinite number of chemical structures and conformational properties. If the role of hydration content is also taken into account, it can be assumed that additional variability may occur.[1] Hydrocolloids are a special class of polysaccharides that contain many hydroxyl groups and therefore can bind water molecules.[2]

Xanthan gum (XG) is an extracellular hydrocolloid of high molar mass (10^6–10^7 Da) which is secreted by the bacterium, *Xanthomonas campestris*.[3,4] The XG backbone consists of a β-1,4-glycosidic bond-linked main chain and a trisaccharide side chain successively containing D-mannose (*b*-1,4), D-glucuronic acid (*b*-1,2) and a terminal D-mannose which contains a pyruvic acid residue linked *via* a keto group to the 4 and 6 positions.[5] It is an anionic polyelectrolyte whose charge originates from the side-chain mannose group and glucuronic residues.[3,6] XG is used in a wide range of applications in the food industry[7–9] and biomedicine.[5,10] As a natural polysaccharide, XG offers some very important advantages such as biodegradability, biocompatibility, and nontoxicity.[11–13]

Water plays a vital role in biological processes and is essential to life and human activity. This is because water significantly affects the catalytic chemical reactions of biopolymers and also acts as a medium that determines the dynamics and structure of biopolymers.[14–17] During the last few years, water and its role in the functionality of biopolymers have attracted much attention. The effect of water on biopolymers' viscoelasticity, glass transition, and origin of water–carbohydrate interactions is still of particular interest.[3] When a polymer is in a glassy state, the rotation around bonds between successive monomers in the polymer backbone is impossible. Therefore, the backbone remains rigid and the viscosity of the system is very high at $\sim 10^{12-13}$ Pa s. The addition of water

[a] *Physics Department, National Technical University of Athens, Iroon Polytechneiou 9, Zografou Campus, Athens, 15780, Greece. E-mail: akyrits@central.ntua.gr*
[b] *Theoretical and Physical Chemistry Institute, National Hellenic Research Foundation, 48 Vassileos Constantinou Avenue, 11635, Athens, Greece*

† Electronic supplementary information (ESI) available. See DOI: https://doi.org/10.1039/d3cp04643e

lowers the glass transition temperature (T_g) as water acts as a plasticizer that enhances the mobility of the macromolecules. However, for many ''ordered'' biopolymers (polysaccharides and globular proteins), a clear glass transition is not always observed through calorimetry or the transition step is very broad.[3,18,19] However, there is no doubt anymore that biopolymers behave the same as synthetic high MW polymers.[20]

It is well established that water molecules in close proximity to biomolecules significantly affect the morphology and dynamics of the macromolecules, while the hydrogen bond (HB) network they form and participate in differs remarkably as compared to that of bulk water. Therefore, the properties of this so-called interfacial or hydration water may reveal specific features of water–polymer interactions.[15,21–25] Among other issues, the non-freezing fraction of adsorbed water,[18,26,27] the confinement of water molecules[28,29] and the process of ice formation at sub-zero temperatures and the dynamics in partially crystallized water mixtures[30–37] are topics that provide insight into the properties of hydration water. Especially for polysaccharides, it is known that a small amount of water significantly affects the T_g of the hydrated polysaccharide by disrupting inter-molecular hydrogen bonds. In addition, it is suggested that when water molecules act as plasticizers, some degree of alignment of the saccharide units is induced (for water contents up to 25%, which is nonfreezing water).[21,25,38]

Over the last few years, there has been a significant increase in the number of studies concerning XG in aqueous solutions, whereas the order–disorder transition of XG has been widely discussed in the literature.[9,39–44] In contrast, only a limited amount of work about the glass transition and other thermal transitions of XG gum can be found in the literature. Yoshida *et al.*[45] studied the phase transitions of the XG–water system using differential scanning calorimetry and reported that the glass transition was found below −73 °C in samples with water content (h_d) between 0.4 and 2.0 (on a dry basis). Another transition has been also found in the high-temperature range (~30 °C, depending on the h_d) that was attributed to the transition from the mesophase to the isotropic liquid state and was detected only in the samples with low water content. In the same context, another work on XG gels reported that a sol–gel transition was observed in the temperature range of 47 °C depending on the molecular weight.[39] The glass transition was also found at temperatures below −73 °C in samples with high water contents, the T_g being decreasing with increasing h_d and reached a minimum at h_d = 0.5. As far as we are aware, this work includes the only phase diagram of the XG gum-water system including the glass-transition, cold-crystallization temperature, melting temperature, and liquid–crystal–liquid transition temperature that has been reported so far. Some other works[46] are in line with the concept that T_g decreases with an increase in water content, as moisture acts as a plasticizer and significantly alters the T_g in amorphous solids but disagree on the values of T_g (in the aforementioned work, T_g varied from −16 °C to −23 °C with increasing water content). In contrast, Raschip *et al.* also worked on XG–water systems in a wide range of hydrations but no clear glass or melting transitions associated with XG were observed over the temperature range of the experiments (from −60 °C to +120 °C).[47] Finally, Kocherbitov *et al.*[48] studied the hydration properties of XG gum and used a modulated DSC method over a temperature range from −40 °C to +120 °C to detect thermal transitions and reported that the glass transition of dry XG gum is at 60 °C.

Given the above information, there are some controversial results regarding even the existence of a glass to liquid transition or the water content dependence of T_g in XG gum. Therefore, the aim of the present work is to study the thermal transitions of XG and the effects of hydration over a wide range of temperature and water content using differential scanning calorimetry (DSC) and broadband dielectric spectroscopy (BDS) techniques and the investigation of the organization of the absorbed water within the polysaccharide. To the best of our knowledge, it is the first study on XG molecular mobility and hydration properties over a wide range of temperature and water content using different experimental techniques.

2. Experimental

2.1. Materials and sample preparation

XG gum from Xanthomonas Campestris was purchased from Sigma-Aldrich (product number G1253). The molecular weight is estimated to be 10^6 Da. For both DSC and BDS experiments, the different hydration levels of the samples, which were in the form of compressed pellets, were achieved by exposure to saturated atmospheres of salt solutions of specific relative humidity, RH (33, 65, 75, 85, 95, and 98%) in sealed jars for 5–6 days to equilibrate to constant weight. We should clarify that the RH of air is defined as the ratio of air vapor pressure to its saturation vapor pressure.[49] The hydration level of the samples is expressed in terms of water fraction, h_w, on a wet basis, using the following equation (eqn (1)):

$$h_w = \frac{m_{water}}{m} \quad (1)$$

where m is the mass of the hydrated sample, $m_{water} = m - m_{dry}$ is the mass of water inside the sample and m_{dry} is the mass of the dry sample. Masses were measured using a Bosch SAE 200 balance with 10^{-4} sensitivity. The hydrations (h_w) that have been achieved were between 0.07 and 0.70. Complete dehydration of the samples was achieved by storing them in a sealed jar containing phosphorus pentoxide for 6 days.

2.2. Differential scanning calorimetry (DSC)

DSC experiments were performed using a TA Q200 series DSC instrument. High-purity helium was the purge gas (selected flow was 25 mL min^{-1}) and indium was used for calibration regarding temperature and enthalpy calculations. Measurements were performed on samples of ~15–20 mg using standard Tzero aluminum pans and aluminum hermetic lids to avoid the evaporation of water inside the samples. DSC standard scans were performed at a cooling/heating rate of 10 °C min^{-1}, while the temperature range was from room temperature (~25 °C) to −150 °C (cooling) and *vice versa* (during heating).

In addition, for temperature modulation DSC (TMDSC) runs, an amplitude ±1 °C with a period of 60 s and a heating rate of 2 °C min^{-1} were selected, while the temperature range was from −100 °C to 100 °C. T_g was estimated using the "half extrapolated tangents" method using TA Universal software, while enthalpies of crystallization and melting, ΔH_{cr}, ΔH_m respectively, were calculated by integrating the area of each peak.

2.3. Broadband dielectric spectroscopy (BDS)

For BDS measurements, the hydrated samples were placed between finely polished round electrodes (brass plates) forming a planar capacitor of 10 mm diameter. The complex dielectric function (dielectric permittivity) $\varepsilon^*(f) = \varepsilon'(f) - i\varepsilon''(f)$ was determined as a function of frequency (f) in the range 10^{-1} to 10^6 Hz at temperatures from −150 °C to 40 °C on heating in steps of 10 °C using a Novocontrol Alpha analyzer. Dielectric isochronal measurements were also performed during cooling at three preselected frequencies (10^3, 10^4 and 10^5 Hz) in order to monitor any crystallization event that may occur. The temperature was controlled to better than 0.5 °C employing a Novocontrol Quatro cryosystem.

Fitting results

To evaluate and interpret dielectric behavior most effectively, raw data were analyzed by fitting model functions. More specifically, the Havriliak–Negami (HN)[50–52] equation (eqn (2)) was used for the analysis,

$$\varepsilon^*(f) = e_\infty + \frac{\Delta\varepsilon}{\left(1 + \left(\frac{if}{f_0}\right)^{a_{HN}}\right)^{\beta_{HN}}} \quad (2)$$

where f_0 is the characteristic frequency related to the frequency of the maximum ε'', ε_∞ represents the value of ε' for $f \gg f_0$, $\Delta\varepsilon$ is the dielectric strength (magnitude), and α_{HN} and β_{HN} are the shape parameters of relaxation for the width and symmetry, respectively.

3. Results and discussion

3.1. Differential scanning calorimetry (DSC)

In Fig. 1, DSC curves obtained during cooling (a) and heating (b) are presented. The inset graph in (a) illustrates the crystallization events of the samples with the highest hydration levels (h_w = 0.36 and h_w = 0.70). It is worth mentioning that all the samples with low levels of hydration (h_w = 0.07–0.27) did not exhibit water crystallization. Therefore, there was an amount of water inside the samples that did not crystallize at subzero temperatures (Table 1). The non-freezing water is the water fraction that does not participate in ice formation and is estimated by employing eqn (3):

$$h_{non\text{-}fr} = h_w - h_{cr\text{-}w} \quad (3)$$

where $h_{cr\text{-}w}$ is the water fraction that crystallizes and is determined by the relation $h_{cr\text{-}w} = \frac{\Delta H_m}{\Delta H_0}$ with ΔH_0 = 333.5 J g^{-1} being the enthalpy of melting of hexagonal bulk ice.[53,54]

With respect to the heating curves in Fig. 1(b), it can be seen that ice melting peaks are detected only for two samples, as expected, while an endothermal step is barely seen in some curves at the selected scale. To distinguish the step for each curve, one needs to focus on the suitable temperature range.

Fig. 2(a) represents DSC heating curves in the glass transition temperature region. Regarding water and its effect on glass transition, it acts as a strong plasticizer, facilitating the mobility of the polymeric chains resulting in a gradual and steady decrease of T_g as water content increases. The dotted lines denote either the onset and final temperature of the endothermic step or the temperature where the signal deviates from the baseline of each heating curve. Both the dry sample and the hydrated samples with the low water contents (h_w = 0.07 and 0.17) do not seem to exhibit glass transition in the temperature range of the other samples. Therefore, for the aforementioned samples along with the dry sample, and to ensure whether glass transition exists or not, apart from standard DSC runs,

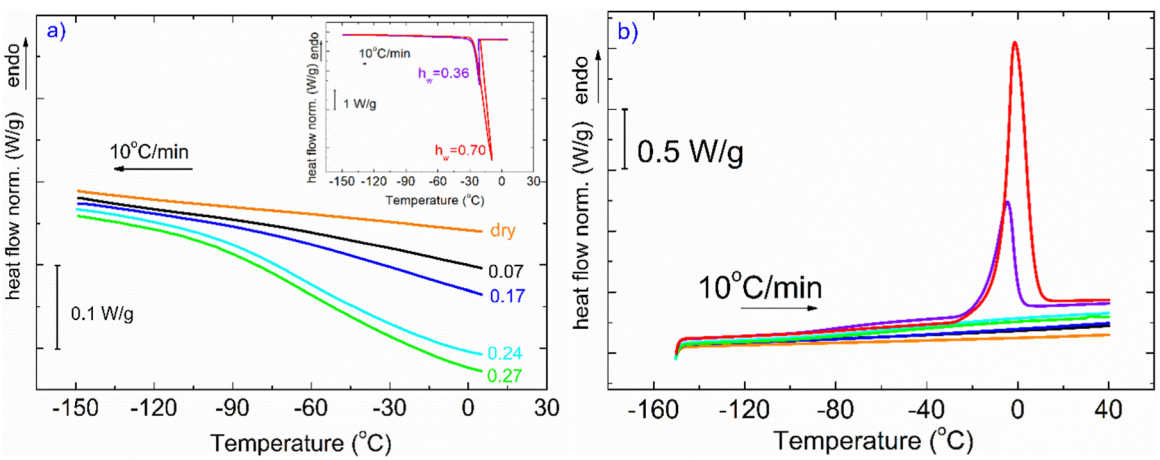

Fig. 1 (a) Comparative DSC cooling curves of XG samples at various hydration levels. The inset cooling curves correspond to the samples for which water crystallization occurs during cooling (h_w = 0.36 and 0.70). (b) DSC heating curves for all the XG samples. Melting of ice occurs only for the two samples with the highest hydration values. The heat flow (in mW) has been normalized to the sample mass (W g^{-1}) in all standard DSC scans. Orange: dry, black: h_w = 0.07, blue: h_w = 0.17, cyan: h_w = 0.24, green: h_w = 0.27, purple: h_w = 0.36, red: h_w = 0.70.

Table 1 Materials under investigation and characteristic values

h_w	T_g (°C) (±0.5)	ΔC_p (J g^{-1} °C^{-1}) (±0.02)	T_m (°C) (±0.5)	T_{cr} (°C) (±0.5)	ΔH_m (J g^{-1}) (±1)	ΔH_{cr} (J g^{-1}) (±1)	$h_{non\text{-}fr\text{-}w}$
0	105	0.12	—	—	—	—	—
0.07	50	0.04	—	—	—	—	—
0.17	−23	0.76	—	—	—	—	—
0.24	−46	0.88	—	—	—	—	—
0.27	−57	0.77	—	—	—	—	—
0.36	−81	0.48	−5	−21	54	47	0.20
0.70	−94	0.30	−1	−20	141	134	0.28

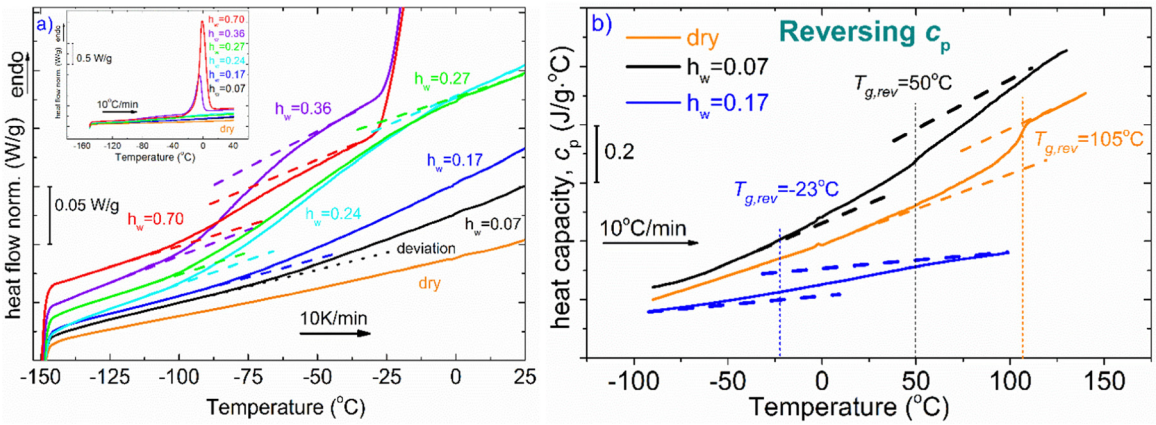

Fig. 2 (a) DSC heating curves focusing on the T_g region are demonstrated. Water seems to act as a strong plasticizer, resulting in a decrease in T_g with increasing water content. (b) Results from temperature-modulated DSC measurements that were performed to separate the thermal events and especially, glass transition, for the dry sample and the two samples with the lowest water content (h_w = 0.07 and 0.17). The lines represent the reversing C_p.

temperature modulation DSC (TMDSC) experiments were also performed. This option provides improved sensitivity especially for detecting weak transitions because it measures not only the total heat flow (as in traditional DSC) but also its reverse heat capacity component separating this contribution from others of kinetic nature. Interestingly, the T_g endothermic step is recorded for the dry sample at 105 °C (Fig. 2b). In the same figure, we present the corresponding signal for the samples with h_w = 0.07 and 0.17. It is remarkable that a small amount of water results in a decrease of T_g by ∼55 °C. With respect to the other samples, the existence of the endothermic step that is associated with the glass transition of the polysaccharide is clearer for the samples with h_w = 0.24 and 0.27 (Fig. 2a). In Table 1, we summarize the characteristic values from all the events that have been recorded during DSC scans.

The phase diagram of Fig. 3(a) was drawn using the data from Table 1. The graph gives information on the water content dependence of T_g, crystallization and melting temperatures, T_{cr}, and T_m respectively. It can be observed that T_g follows a downward trend and decreases sharply as the hydration level increases up to the value of h_w = 0.36 which corresponds to a RH of 95%. This behavior of the experimental data follows the trend indicated by the Fox equation[55] (eqn (4))

$$\frac{1}{T_g} = \frac{w_{(\text{XG dry})}}{T_{g,(\text{XG dry})}} + \frac{w_{(\text{water})}}{T_{g,(\text{water})}} \quad (4)$$

which connects the T_g of the sample with the T_g and weight fraction, w, values of each component. As can be seen in Fig. 3a, the fitting is very good, taking into account the data up to water content h_w = 0.27; however, it should be mentioned that the parameter T_g (water), *i.e.*, the T_g of pure water, has the value of 110 K, below the value of 135 K which is the suggested value for bulk water.[56–58] Fig. 3(b) describes how hydration water affects T_g and heat capacity increment at the glass transition, ΔC_p. In general, ΔC_p increases with h_w in the water content range where water molecules act as plasticizers and decreases with increasing h_w at higher hydration levels.

3.2. Broadband dielectric spectroscopy (BDS)

In Fig. 4, the temperature dependence of the real part of dielectric permittivity, (ε'), during cooling and heating for all the samples recorded at $f = 10^5$ Hz is presented. It can be observed that the coincidence of the response during cooling and heating is perfect in the whole temperature range only for the samples with the lower hydration levels (h_w = 0.07–0.24). As for the samples with higher hydration levels (h_w = 0.27–0.70), the signal does not perfectly match during cooling and heating, indicating some rearrangements of water organization with temperature changes. More specifically, for the samples with h_w = 0.36 and h_w = 0.70, we observe a sudden drop of ε' during cooling at about −20 °C, which denotes a first-order transition (ice formation). However, below that temperature, the signals

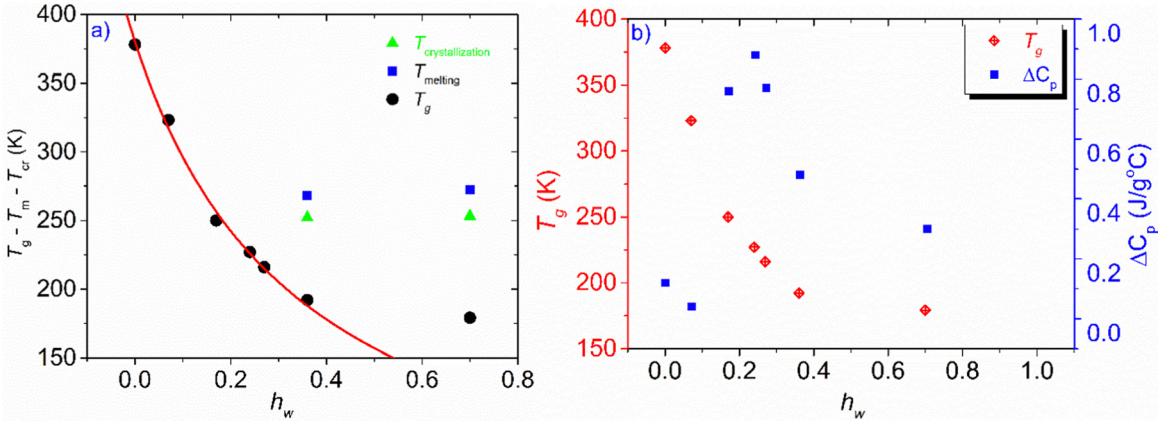

Fig. 3 (a) Phase diagram of the h_w dependence of T_g, T_{cr}, and, T_m, (b) hydration water dependence of T_g and heat capacity variation at the glass transition, ΔC_p. The red solid line represents the result of the fitting procedure using the Fox equation.[55] For a fully hydrated sample (h_w = 1), *i.e.*, pure water, the T_g value was estimated to be 110 K, below the generally accepted value which is ~135 K.

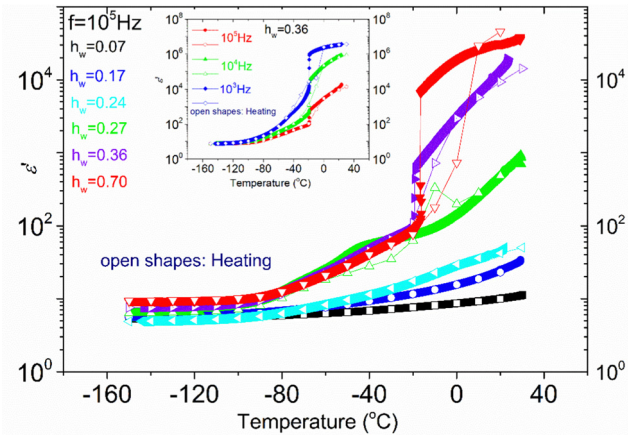

Fig. 4 ε' recorded isochronally at the frequency $f = 10^5$ Hz during cooling (closed symbols) and recorded isothermally during heating (open symbols) for all the samples. In the inset graph, we focus on the sample with h_w = 0.36 and we show the sudden drop of ε' in all three frequencies (10^3, 10^4, 10^5 Hz) at the same temperature (−20 °C), which denotes that a first-order transition occurs during cooling (ice formation).

merge. On the other hand, the response of the sample with h_w = 0.27 deviates at about 3 °C during cooling and the two responses (during cooling and heating) merge again at about −70 °C, below the calorimetric glass transition temperature detected during calorimetric measurements (−57 °C). In the low-temperature range, the signal is almost identical for all the samples during cooling and heating as expected because polysaccharide chains are immobilized. In the inset of Fig. 4, data for the sample with h_w = 0.36 are presented for two additional frequencies ($f = 10^4$ and 10^3 Hz), showing the existence of the sudden drop of ε' at each curve, *i.e.*, a drop that is independent of the monitoring frequency. This fact confirms that a first-order transition (ice formation) occurs during cooling, not only for this sample but also for the sample with the highest hydration level (h_w = 0.70).

Fig. 5(a) illustrates ε' and Fig. 5(b) ε'', isothermal data, for the dry XG sample. The data from this sample were chosen to be presented separately so that the information is not eliminated due to scaling. In Fig. 5(a) we can see that the dielectric response is in general low but there is an upward trend with increasing temperature. In Fig. 5(b), it can be seen that at low frequencies and for temperatures above 50 °C, a wide and symmetric peak can be detected within the experimental window range; however, values are rather low confirming that the dielectric response of this sample is quite low. Nevertheless, since this sample does not contain water, we can assume that this peak (centered at about 20 Hz at −30 °C) corresponds to a relaxation of side polar groups of the polysaccharide that shifts to higher frequencies with increasing temperature (process I_{dry}).

In the next part of this section, we deal with all the other samples except the dry one. At T = −110 °C (Fig. 6a), we can see that there is only a slight increase of ε' for the samples with h_w = 0.07–0.24, whereas ε' increases more rapidly for the rest of the samples (h_w = 0.27–0.70) as the water content increases. Looking at the dielectric loss shown in Fig. 6(b), it is observed that at −110 °C, at least one relaxation process has already entered the experimental window for all the samples, while for those with the highest hydration levels, at least two relaxation processes have been detected. For the three samples with the lowest water content (h_w = 0.07, 0.17, 0.24), a wide and symmetric peak is detected at the lower part of the frequency range centered at about 0.1, 1, and 10 Hz, respectively (process I). Concerning the sample with the next highest water content (h_w = 0.27), the spectra become more complex: the process I is still recorded but with higher intensity, while another faster relaxation process (process Ia) could be seen at higher frequencies, centered at about 10^3 Hz as revealed by the fitting procedure. For both samples with the highest water content, the spectra are rather complex: the peak that is related to the relaxation of ice formed during cooling was detected at about 1 Hz (h_w = 0.36) and 15 Hz (h_w = 0.70). The fitting procedure in the spectrum of the sample with h_w = 0.36 has also revealed another relaxation process, (process I) though its peak is not clear due to the superposition with the ice relaxation peak.

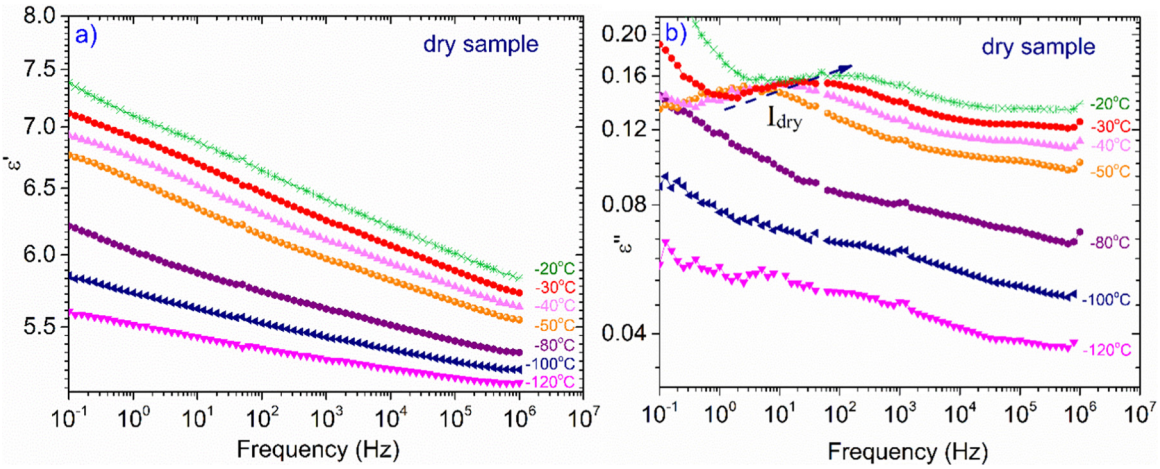

Fig. 5 Frequency dependence of (a) ε', and (b) ε'' for the dry XG sample at selected temperatures indicated in the plots.

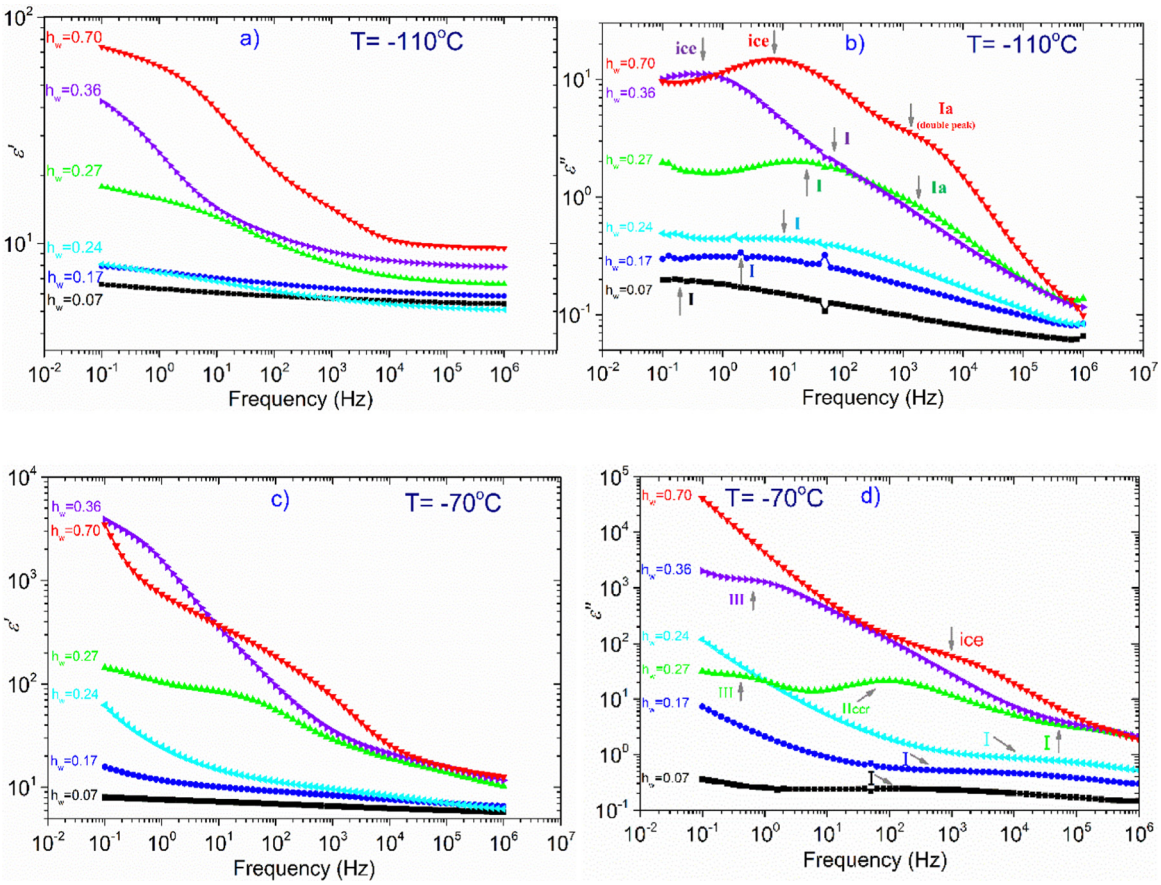

Fig. 6 The frequency dependence of ε', and ε'' at two indicative temperatures, (a) and (b) −110 °C, (c) and (d) −70 °C. Symbols at (a)–(d): squares: h_w = 0.07, circles: h_w = 0.17, triangles left: h_w = 0.24, triangles up: h_w = 0.27, triangles right: h_w = 0.36, triangles down: h_w = 0.70.

In addition, looking at the spectrum of the sample containing the maximum amount of water, a double (as revealed by the fitting) and fast relaxation process can be observed, centered at about 2k Hz (process Ia).

At −70 °C, (Fig. 6c) the dielectric permittivity increases with h_w except for the sample with the lowest water content (h_w = 0.07) whose signal remains almost unchanged in the whole frequency range. Regarding the sample with the next higher water content (h_w = 0.17), there is only a slight increase in the low-frequency regime, meaning that there is a limited number of charged species that can follow the changes of the electric field and therefore contribute to the polarization

process. The response of the next sample (h_w = 0.24) follows an upward trend, whereas this increase is more significant at frequencies lower than 50 Hz. The dielectric loss spectra (Fig. 6d) of the three aforementioned samples revealed the same process (I) recorded at −110 °C, with the difference that the peak of the relaxation is shifted to higher frequencies, as expected. Of particular interest is the behavior of the sample with h_w = 0.27 because a Vogel–Tammann–Fulcher (VTF) relaxation process (namely process IIccr) has been recorded during BDS measurements. As can be seen in Fig. 6(c), ε' increases already in the high-frequency range, while a step is detected between 10^1 and 10^3 Hz. This step in the dielectric permittivity spectrum is accompanied by a peak in the same frequency region in the dielectric loss spectrum (Fig. 6d). As it will be shown later, this peak is probably related to the conduction current relaxation mechanism. As for the two samples with the highest water content (h_w = 0.36, 0.70), we can see that ε' increases sharply at low frequencies implying the activation of strong, interfacial polarization processes. It is worth mentioning that in the low frequency range (0.1–1 Hz), another process has been recorded for the samples with h_w = 0.27 and h_w = 0.36 (process III).

In Fig. 7, we focus on the sample with h_w = 0.27. Though this particular sample does not exhibit water crystallization events either in the DSC measurements (Fig. 1a and b), or in the isochronal dielectric measurements during cooling (Fig. S3 in ESI†), interestingly, it behaves similarly to the samples that crystallize upon cooling. More specifically, in Fig. 7(a) is shown the temperature dependence of ε', recorded at frequency f = 1 MHz, for all hydrated samples and obviously ε' values of the sample with h_w = 0.27 follow an upward trend during heating similar to the two samples with the highest water content, *i.e.*, with the samples that contain the ice phase. It is worth mentioning that this sample exhibits a strong polarization process, called process IIccr, which is shown in Fig. 7b. This process can be monitored already at −90 °C and so clearly only for this water content. In Fig. S4 in ESI,† are shown the real, ε', and imaginary, ε'', parts of the dielectric permittivity recorded in the temperature range of −70 °C up to −10 °C, for the samples with h_w = 0.24, 0.27 and 0.36, respectively. For the comparison, it is obvious that process IIccr is observed only for water contents around 0.27. This process may be related to specific features of the hydrogen bond network of absorbed water, just before the formation of the crystalline phase (water phase separation) that occurs at higher amounts of adsorbed water. In the following section, we will deal with this polarization process.

Fig. 8 illustrates an example of the fitting procedure for two samples with h_w = 0.27 and h_w = 0.70 at −90 °C. For h_w = 0.27, a broad peak (process I) is detected centered at about 10^3 Hz, while a second peak (process IIccr) can be observed at about 10^{-1} Hz. Concerning the other sample with h_w = 0.70, a relaxation peak centered at about 200 Hz, related to the ice relaxation, is observed together with a second weak process (relaxation Ia_{ii}) centered at about 10^4 Hz. This process can be resolved at very low temperatures (low-T double peak).

We now turn our attention to the time scale of all the relaxation processes recorded and the corresponding dielectric strength $\Delta\varepsilon$. Fig. 9 outlines the results of the analysis of BDS spectra obtained on the samples with low hydration levels (dry up to h_w = 0.27) by showing the Arrhenius plot for the mean relaxation times of all relaxation processes detected (a), as well as the corresponding diagram for their dielectric strength (b). Starting with the Arrhenius plot in Fig. 9(a), it can be seen that process I exhibits Arrhenius-like temperature dependence and is detected in all the samples. The fact that this relaxation is observed not only in the hydrated samples but also in the dry ones, allows us to conclude that this is a secondary relaxation process of polar-hydrophilic groups of the polysaccharide, that is, this process is related either to the local main chain dynamic or/and to the side group motions (β-relaxation). Our data reveal a strong impact of water molecules on the dynamics of process I. Indeed, the process becomes faster with increasing water content, especially for low water contents, while its magnitude increases with increasing water content. Many dielectric studies on hydrated polymers

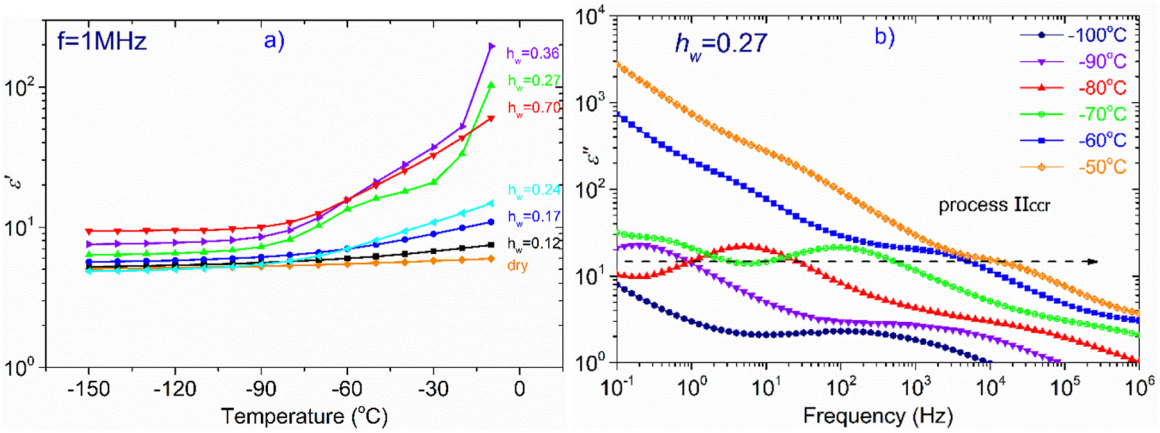

Fig. 7 (a) Temperature dependence of ε' at f = 1 MHz, (b) ε'' for the sample with h_w = 0.27 at selected temperatures. The arrow is a guide to the eye and indicates the shift of the process IIccr peak to higher frequencies with increasing temperature.

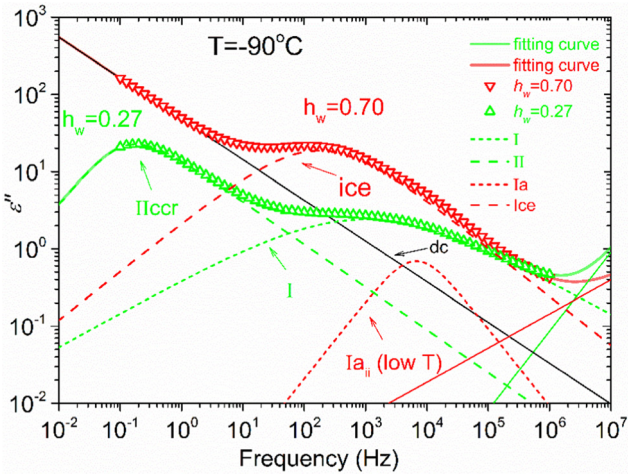

Fig. 8 Dielectric loss, ε'', as a function of frequency at −90 °C for the samples with h_w = 0.27 and h_w = 0.70. Concerning the first sample, the green short dash line refers to process I, while the green long dash line corresponds to process IIccr. As for the second sample, the dashed line shows the peak corresponding to ice dielectric relaxation. The short dash line represents the Ia_{ii} (low temperature) fast relaxation process. For both samples, the solid lines represent the sum of all contributions (fitting curves). The solid lines at the right part of the graph represent the low-frequency wing of the processes Ia for the sample with h_w = 0.27 and Ia_i for the sample with h_w = 0.70.

revealed the existence of similar relaxation processes that are based on the local mobility of the matrix and are enhanced by the absorbed water molecules becoming faster and increasing in strength gradually with the increase of water content. The evolution of this low temperature relaxation with the increasing hydration level has revealed an interplay between a local dielectric relaxation mode of polar groups on the macromolecular chains interacting with water molecules and a relaxation process originated in the reorientation of water molecules themselves (the main secondary relaxation process of water or ν-process) above a critical water content.[59–63]

For the samples with higher water fractions, a saturation of plasticization is observed, *i.e.*, the first hydration shell has been established. For comparison purposes, in Fig. 9(a), we have added the bottom limit for the time scale of the secondary process in bulk water (ν-process).[57] If we focus on the sample with h_w = 0.27, we can see that there is an additional activated process (process IIccr) that shows (VTF) temperature dependence, which is typical of cooperative relaxation processes. Nevertheless, given that the calorimetric T_g was found in different temperature ranges (as is indicated in Fig. 9a), this process could not be associated with α-relaxation. It is also interesting to comment that the dielectric strength of process IIccr (Fig. 9b) increases with decreasing temperature close to the calorimetric T_g. As for the low-temperature relaxation (process Ia), it follows the Arrhenius law with a very low activation energy (0.11 eV) and its dielectric strength is rather low. We speculate that this process is related with a particular form of water organization but more experimental studies are needed for the clarification of the origin of this peak. It is worth mentioning that similar relaxations have been recorded in other biopolymers.[59] To further investigate the origin of process IIccr, the corresponding relaxation times were calculated using the following empirical Barton-Nakajima–Namikawa (BNN) relation (eqn (5)):

$$\tau_{BNN} = \frac{p\Delta\varepsilon\varepsilon_\infty}{\sigma_0} \quad (5)$$

where $\Delta\varepsilon$ is the dielectric strength of process IIccr at a given temperature, σ_0 is the dc conductivity at this temperature and ε_∞ is the dielectric constant at high frequencies. In eqn (5), p is usually close to 1.[60,64,65] The BNN polarization process may appear due to charge accumulation in media that are characterized by structural local disorder and exhibit long

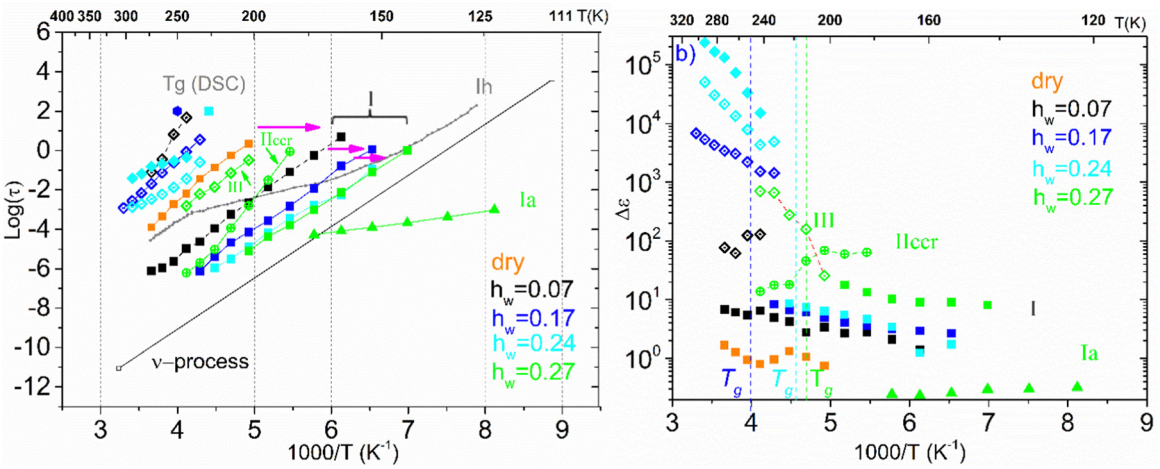

Fig. 9 (a) Arrhenius plots of mean relaxation times of processes recorded on the samples with low hydration levels (h_w = 0–0.27). At low temperatures, processes Ia (triangles) and I (squares) can be seen. At the high temperature, regime process III is recorded (rhombuses). Furthermore, process IIccr (circles with a cross) of the sample with h_w = 0.27 which follows a VTF temperature dependence can been seen. For comparison, we have also added the bottom limit for the time scale of the secondary process in bulk water (ν-process), whereas the dotted line shows the dielectric response of hexagonal ice I_h. (b) The corresponding dielectric strength of the processes.

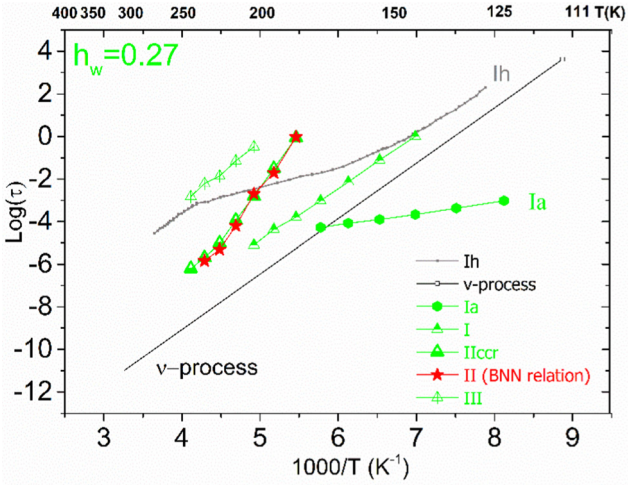

Fig. 10 Arrhenius plots for the mean relaxation times for the sample with h_w = 0.27. Using the red stars, we present the time scale of the corresponding BNN-type polarization process.

range charge conduction (dc conductivity). The calculated τ_{BNN} values together with the experimental relaxation time values estimated by our fitting process for the specific relaxation process are shown in Fig. 10. Interestingly, the coincidence of the calculated values and the experimental points is very good indicating that, indeed, process IIccr is related to such a conductivity current relaxation mechanism. At higher temperature, another relaxation process is recorded (process III) that follows the Arrhenius law and its dielectric strength increases with increasing temperature.

Concerning the two samples that contain ice phases and have the highest hydration levels (h_w = 0.36 and 0.70), Fig. 11 illustrates the Arrhenius plot for the mean relaxation times (a), and the dielectric strength of the processes recorded (b). It seems that two almost identical fast relaxation processes are recorded for the sample with h_w = 0.70 (marked as Ia_i and Ia_{ii}). These processes have a time scale similar to process Ia that has been recorded for the sample with h_w = 0.27 (Fig. 9a). Considering process Ia_{ii}, it has the same activation energy as Ia (Table 2). For both samples, process II is related to the relaxation of ice that has been formed during cooling and is monitored during BDS measurements. For comparison, in Fig. 11(a) is also shown the trace of the dielectric relaxation time reported in the literature, illustrating the relaxation process in bulk hexagonal ice, I_h.[59,66] As for the sample with h_w = 036, except for the aforementioned process II, we can also see another faster relaxation (namely process I), which might be the same secondary relaxation process of polar-hydrophilic groups that has been recorded for all the samples with lower hydration levels (dry up to h_w = 0.27). Interestingly, an additional process has been recorded (process III) with a trace that coincides with that of the same process of the sample with h_w = 0.27.

Table 2 Activation energy, E_{act} (eV), of the Arrhenius equation for the relaxations monitored in all the samples. (an uncertainty of ±0.01 eV is estimated using the fitting procedure)

	Process					
h_w	I_{dry}	I	Ia	Ia (i)	Ia (ii)	ice
dry	0.74					
0.07		0.66				
0.17		0.54				
0.24		0.52				
0.27		0.50	0.11			
0.36		0.44				0.34
0.70				0.19	0.11	0.42

In Fig. 11(b), we present the corresponding dielectric strength for each process that has been recorded. We can see that the values of Δε for process I of the sample with h_w = 0.36 are almost coincident with the values of the same process that has been recorded in the samples with low hydration levels (Fig. 9b). Processes Ia_i and Ia_{ii} are characterized by almost constant Δε values in the low-temperature range. However, a gradual decrease is observed at −110 °C and −90 °C,

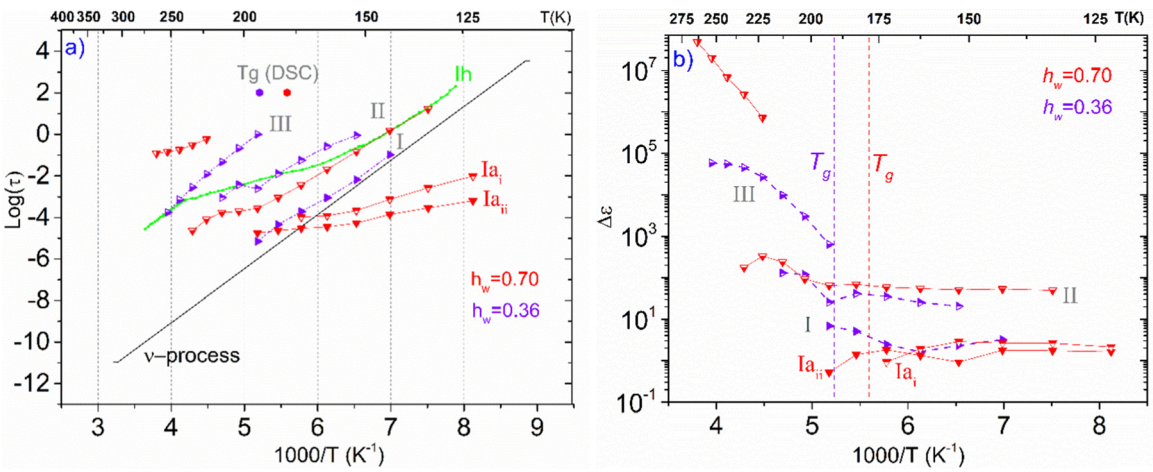

Fig. 11 (a) Arrhenius plots of mean relaxation times of processes recorded on the samples with the highest hydration levels (h_w = 0.36 and 0.70), (b) the corresponding dielectric strength Δε.

respectively, for the dielectric strength of process II (ice relaxation), it is more or less stable with $\Delta\varepsilon$ values $\sim$60–80, which are typical values for ice relaxation. In the high-temperature range, a fluctuation of the values is observed. $\Delta\varepsilon$ values of process III become higher with increasing temperature like the corresponding values of this process for the sample with h_w = 0.27, but with higher values.

In Table 2, the activation energies of all processes recorded are presented. We should highlight that the values for processes I_{dry} and I are quite high for a local relaxation of side chain hydroxyl groups. Nevertheless, similar values have been previously reported in the literature. More specifically, Montes *et al.* who studied secondary relaxations in amorphous cellulose reported E_{act} = 85 kJ mol^{-1} (0.88 eV), which decreases with increasing water content *e.g.*, E_{act} = 60 kJ mol^{-1} (0.62 eV) for the sample with water content 6 w/w%.[67] According to Heijboer, these activation energies are too high to ascertain that only lateral groups are responsible for these relaxations and it is clear that these processes could not correspond to the glass transition. Therefore, they may also be associated with localized motions of the main chain.[68,69] Furthermore, Panagopoulou *et al.* reported E_{act} = 0.67 eV for the secondary relaxation on the dry BSA sample, a value which also decreases with increasing water content.[59] At this point, it is useful to mention that given that there is a strong correlation in the dynamics of the polysaccharides and of biopolymers in general, the different modes of molecular motions are not independent of each other and it is therefore difficult to assign the relaxation process found experimentally to the corresponding orientational processes on the molecular level.

From the frequency dependence of the real part of conductivity in $\sigma'(f)$ plots, like those shown in ESI,† Fig. S1(a), we are able to estimate the dc conductivity values which allow us to create the dc conductivity Arrhenius plot presented in Fig. 12 by plotting σ' values at the frequency in which a dc plateau is observed at a given temperature, as a function of 1000/T, for each isothermal curve. There are some interesting features worth mentioning. To start with, a low temperature and mid-frequency conduction process that is of Arrhenius type is recorded in the sample with the highest water content (h_w = 0.70) with low activation energy (E_{act} = 0.16 eV). This process can be attributed to the crystalline ice phase, *i.e.*, conducive paths are created *via* the bulk-like ice structures. At higher temperatures, we can see that another dc conduction process is established in the low frequency range. This dc conduction process is recorded similarly in all the samples with water content $h_w \geq 0.27$, at least in the temperature range from -60 to -10 °C. For all the samples, this process is characterized by almost the same activation energy, E_a = 0.78–0.90 eV. This behavior allows us to assume that similar conduction processes for the charge carriers exist in all the samples, at this temperature range, providing the existence of a specific network of the adsorbed water molecules. Given that we have recorded a low-temperature conduction process that can be associated with the presence of the ice phase in the sample with h_w = 0.70, we assume that above -80 °C (approximately), similar charge transport processes are possibly activated *via* the HB network of the existed non-freezing water fraction that is almost constant (0.20–0.28) irrespective of the total water content. Such rather high apparent activation energies have been also observed in other water containing systems[53,70,71] and may be attributed to the specific features of the HB network of the interfacial water and the particular mechanism for the proton transfer.[72,73]

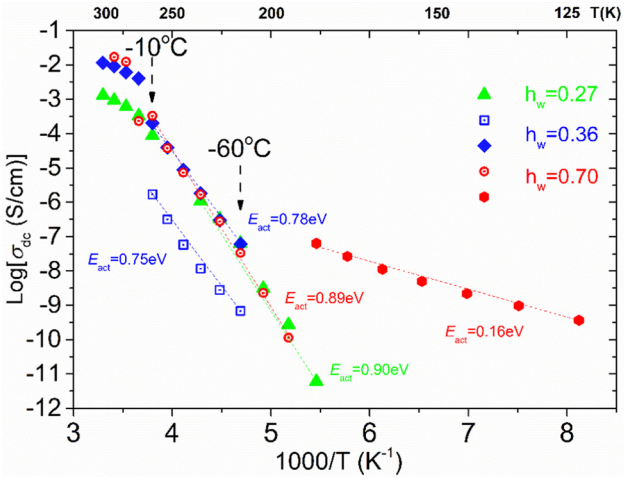

Fig. 12 Arrhenius plots for the dc conductivity recorded in the three samples with the highest h_w. The dash lines are a guide to the eye showing the temperature dependence of the conductivity processes. A low temperature process has been recorded for the sample with the highest water content (h_w = 0.70). At higher temperatures, another conductivity process can be seen which is interestingly almost identical for all the samples. For the sample with the second highest water content, (h_w = 0.36), another process has been detected but with lower conductivity values.

4. Conclusions

This work aimed to study XG gum, in terms of glass transition and molecular mobility over a wide range of hydration (h_w varied from 0 to 0.70) by employing DSC and broadband BDS techniques. More specifically, DSC measurements were carried out to investigate thermal events and to estimate T_g. BDS experiments were conducted to study the dielectric behavior of the polysaccharide and the activated conduction processes and the way water affects the aforementioned processes.

At the hydration levels of this study, we found that the samples under investigation contain either only non-freezing water, or an additional amount of water that can crystallize during cooling. This means that depending on the water content, there is an amount of bound water, clustered water and bulk-like water that can form a separate phase at subzero temperatures. The critical water fraction for ice formation was found as h_w = 0.35. T_g which is associated with α-relaxation was recorded for all the samples studied during standard DSC experiments. To provide improved sensitivity, and to detect any weak glass transition, apart from the standard DSC scans, we have also performed TMDSC measurements, in particular for the dry one and the two samples with the lowest water contents (h_w = 0.07 and 0.17). These experiments revealed that

though the glass transition was not recorded during standard DSC scans, these samples are also subjected to glass transition. As shown in Table 1, there is a strong water content dependence of T_g, *e.g.*, the dry sample undergoes glass transition at 105 °C, while a very small amount of water (h_w = 0.07) results in a remarkable decrease of T_g by 55 °C. This decrease is expected, as water molecules act as strong plasticizers, and T_g decreases with the increasing water content of the samples.

With respect to the BDS experiments, a secondary relaxation process (namely process I_{dry}, process I) has been detected in all the samples, including the dry one, except the sample with the maximum water content. This finding allows us to assume that this relaxation process is related to the relaxation of polar-hydrophilic groups of the polysaccharide that is being plasticized by water molecules. Consequently, we believe that processes I and I_{dry} can be attributed either to the side groups (D-mannose groups, D-glucuronic acid) or/and to the local motions of the main chain (hydroxymethyl groups –CH_2OH). This interpretation is also driven by the strong plasticization of this particular process by water, which has been observed in biomolecules where the plasticization of the matrix is accompanied by the acceleration of the local molecular mobility. Concerning the sample with h_w = 0.27, a VTF-like relaxation process has been recorded (process IIccr). This process is controlled by the long-range dc conductivity, which is influenced by the conductivity current relaxation mechanism, as shown in Fig. 10 and by using the BNN relationship. A fast but weak process (namely process Ia) has been also recorded for this sample that follows an Arrhenius behavior with low activation energy (0.11 eV) and its origin remains unclear. Another process (III) has been also recorded for this sample that follows an Arrhenius law. As for the two samples with the highest water content (h_w = 0.36 and 0.70), the fitting procedure revealed the peak that is related to ice relaxation. Furthermore, process I, *i.e.*, the same process that has been recorded in the samples with lower h_w, was also identified for the sample with h_w = 0.36, while two additional but low energy processes (Ia_i and Ia_{ii}) have been recorded for the sample with h_w = 0.70. Process III was recorded for the sample with h_w = 0.36 at high temperatures.

Concerning the dc conductivity of the samples, our measurements reveal that two types of long-range charge transport processes are activated. The first one has its origin in the conductive paths that can be formed through the bulk-like ice structures in the low-temperature range ($T < -110$ °C) and are detected only for the sample with the highest water content. Taking into account that the second process was recorded at higher temperatures ($T > -85$ °C) in all the samples with $h_w \geq 0.27$, we conclude that this common charge transport process is realized *via* the HB network of the non-freezing clustered water molecules and its characteristics are independent of the hydration level.

As far as we are aware, it is the first time that XG is studied in terms of glass transition and molecular mobility in a wide range of temperatures, frequencies, and water fractions using DSC and BDS techniques. To conclude, the results of our measurements reveal that the molecular mobility of XG molecules is strongly affected by the presence of water molecules.

Conflicts of interest

The authors have no conflicts of interest to disclose.

Acknowledgements

S. N. T. would like to acknowledge Dr Daniel Fragiadakis from the Naval Research Laboratory, Polymer Physics Section, Washington DC, USA for kindly providing his 'grafity' data analysis software (**https://grafitylabs.com/**).

References

1 E. Westhof, *Water and Biological Macromolecules*, Red Globe Press, London, 1993.
2 D. Saha and S. Bhattacharya, *J. Food Sci. Technol.*, 2010, **47**, 587–597.
3 S. E. Hill, D. A. Ledward and J. R. Mitchell, *Functional properties of food macromolecules*, Aspen Publishers, Gaithersburg, 1998.
4 A. Jeanes, *Food technology*, 1974, **28**, 34–40.
5 D. F. S. Petri, *J. Appl. Polym. Sci.*, 2015, **132**, 42035.
6 X. Hu, K. Wang, M. Yu, P. He, H. Qiao, H. Zhang and Z. Wang, *Biomolecules*, 2019, **9**, 730.
7 A. M. Grumezescu and A. M. Holban, *Handbook of Food Bioengineering, Biopolymers for Food Design*, Academic Press, London, San Diego, 2018.
8 I. A. Challen, in *Food Hydrocolloids*, ed. K. Nishinari and E. Doi, Springer, Boston, MA, 1994, Xanthan Gum: A Multifunctional Stabiliser for Food Products, pp. 135–140.
9 M. Milas and M. Rinaudo, *Carbohydr. Res.*, 1979, **76**, 189–196.
10 D. H. Hanna and G. R. Saad, *Bioorg. Chem.*, 2019, **84**, 115–124.
11 A. Jain, S. K. Singh, S. K. Arya, S. C. Kundu and S. Kapoor, *ACS Biomater. Sci. Eng.*, 2018, **4**, 3939–3961.
12 J. Patel, B. Maji, N. S. Hari Narayana Moorthy and S. Maiti, *RSC Adv.*, 2020, **10**, 27103.
13 W. Lohcharoenkal, L. Wang, Y. C. Chen and Y. Rojanasakul, *BioMed Res. Int.*, 2014, 180549.
14 J. H. Roh, *Macromol. Chem. Phys.*, 2016, **217**, 256–265.
15 D. Laage, T. Elsaesser and J. T. Hynes, *Chem. Rev.*, 2017, **117**, 10694.
16 S. Cerveny and J. Swenson, *J. Chem. Phys.*, 2019, **150**, 234904.
17 G. Kerch, *Int. J. Biol. Macromol.*, 2018, **118**, 1310–1318.
18 A. Panagopoulou, A. Kyritsis, R. Sabater Serra, J. L. Gómez Ribelles, N. Shinyashiki and P. Pissis, *Biochim. Biophys. Acta, Proteins Proteomics*, 2011, **1814**, 1984–1996.
19 H. Jansson and J. Swenson, *Biochim. Biophys. Acta*, 2010, **1804**, 20–26.
20 B. Wunderlich, *J. Therm. Anal. Calorim.*, 2011, **106**, 81–84.
21 T. Hatakeyama, M. Tanaka, A. Kishi and H. Hatakeyama, *Thermochim. Acta*, 2012, **532**, 159–163.
22 P. Pissis and A. Kyritsis, *J. Polym. Sci., Part B: Polym. Phys.*, 2013, **51**, 159–175.
23 S. Kripotou, E. Stefanopoulou, M. C. Martínez, R. M. M. Román, G. Ferrer and A. Kyritsis, *Polymer*, 2019, **178**, 121598.

24 S. Cerveny, F. Mallamace, J. Swenson, M. Vogel and L. Xu, *Chem. Rev.*, 2016, **116**, 7608–7625.
25 M. Grossutti and J. R. Dutcher, *Biomacromolecules*, 2020, **21**, 4871–4877.
26 V. Kocherbitov, *Carbohydr. Polym.*, 2016, **150**, 353–358.
27 M. Fujii, K. Sasaki, Y. Matsui, S. Inoue, R. Kita, N. Shinyashiki and S. Yagihara, *J. Phys. Chem. B*, 2020, **124**, 1521–1530.
28 J. Swenson, *Phys. Chem. Chem. Phys.*, 2018, **20**, 30095–30103.
29 Y. Beilinson, V. Schiller, J. Regentin, J. H. Melillo, A. Greenbaum, T. Antropova, S. Cerveny, M. Vogel and Y. Feldman, *J. Phys. Chem. B*, 2023, **127**, 5128–5140.
30 Q. Wang, X. Huang, W. Guo and Z. Cao, *Phys. Chem. Chem. Phys.*, 2019, **21**, 10293–10299.
31 B. Vijayakumar, M. Takatsuka, K. Sasaki, R. Kita, N. Shinyashiki, S. Yagiharad and S. Rathnasabapathy, *Phys. Chem. Chem. Phys.*, 2023, **25**, 22223.
32 P. Talik and U. Hubicka, *J. Therm. Anal. Calorim.*, 2018, **132**, 445–451.
33 W. G. Liu and K. D. Yao, *Polymer*, 2001, **42**, 3943–3947.
34 N. Shinyashiki, M. Shimomura, T. Ushiyama, T. Miyagawa and S. Yagihara, *J. Phys. Chem. B*, 2007, **111**, 10079–10087.
35 K. Sasaki, A. Panagopoulou, R. Kita, N. Shinyashiki, S. Yagihara, A. Kyritsis and P. Pissis, *J. Phys. Chem. B*, 2017, **121**, 265–272.
36 K. Sasaki, I. Popov and Y. Feldman, *J. Chem. Phys.*, 2019, **150**(20), 204504.
37 J. H. Melillo, E. Nikulina, M. A. Iriarte-Alonso, S. Cerveny and A. M. Bittner, *Sci. Rep.*, 2022, **12**, 16512.
38 A. Průšová, F. J. Vergeldt and J. Kučerík, *Carbohydr. Polym.*, 2013, **95**, 515–521.
39 H. Hatakeyama and T. Hatakeyama, *Thermochim. Acta*, 1998, **308**, 3–22.
40 C. E. Brunchi, M. Bercea, S. Morariu and M. Dascalu, *J. Polym. Res.*, 2016, **23**, 123.
41 A. Gamini, J. de Bleijser and J. C. Leyte, *Carbohydr. Res.*, 1991, **220**, 33–47.
42 T. Sato, T. Norisuye and H. Fujita, *Macromolecules*, 1984, **17**, 2696–2700.
43 T. A. Camesano and K. J. Wilkinson, *Biomacromolecules*, 2001, **2**, 1184–1191.
44 A. Papagiannopoulos, K. Sotiropoulos and A. Radulescu, *Carbohydr. Polym.*, 2016, **153**, 196–202.
45 H. Yoshida, T. Hatakeyama and H. Hatakeyama, *Polymer*, 1990, **31**, 693–698.
46 S. Basu, U. S. Shivhare and A. S. Mujumdar, *Drying Technol.*, 2007, **25**, 1581–1586.
47 I. E. Raschip, I. Yakimets, C. P. Martin, S. S. Paes, C. Vasile and J. R. Mitchell, *Powder Technol.*, 2008, **182**, 436–443.
48 V. Kocherbitov, S. Ulvenlund, L. E. Briggnerb, M. Koberb and T. Arnebranta, *Carbohydr. Polym.*, 2010, **82**, 284–290.
49 F. Kong and R. P. Singh, in *Food and Beverage Stability and Shelf Life*, ed. D. Kilcast and P. Subramaniam, Woodhead Publishing, 2011, **12**, pp. 381–404.
50 F. Kremer and A. Schönhals, *Broadband Dielectric Spectroscopy*, Springer, Berlin, 2002.
51 S. Tatsuoka and H. Sato, *Spectrochim. Acta, Part A*, 2018, **197**, 95–102.
52 S. Havriliak and S. Negami, *Polymer*, 1967, **8**, 161–210.
53 S. Kripotou, K. Zafeiris, M. Culebras-Martínez, G. Gallego Ferrer and A. Kyritsis, *Eur. Phys. J. E.*, 2019, **42**, 109.
54 J. A. Dean, *Lange's Handbook of Chemistry*, McGraw-Hill, New York, 1999.
55 J. C. Lee and M. H. Litt, *Polym. J.*, 2000, **32**, 228–233.
56 S. Capaccioli and K. L. Ngai, *J. Chem. Phys.*, 2011, **135**, 104504.
57 G. P. Johari, A. Hallbruckert and E. Mayert, *Nature*, 1987, **330**, 552–553.
58 P. Lucas, J. Pries, S. Wei and M. Wuttig, *J. Non-Cryst. Solids: X*, 2022, **14**, 100084.
59 A. Panagopoulou, A. Kyritsis, N. Shinyashiki and P. Pissis, *J. Phys. Chem. B*, 2012, **116**, 4593–4602.
60 S. Kripotou, S. N. Tegopoulos, A. Kyritsis, L. O. Cervelló, A. Vallés-Lluch and G. G. Ferrer, *IEEE Trans. Dielectr. Electr. Insul.*, 2020, **27**, 1387–1394.
61 C. Gainaru, A. Fillmer and R. Böhmer, *J. Phys. Chem. B*, 2009, **113**, 12628–12631.
62 A. Panagopoulou, J. V. Molina, A. Kyritsis, M. M. Pradas, A. Vallés Lluch, G. G. Ferrer and P. Pissis, *Food Biophys.*, 2013, **8**, 192–202.
63 S. Capaccioli, K. L. Ngai, S. Ancherbak, P. A. Rolla and N. Shinyashiki, *J. Non-Cryst. Solids*, 2011, **357**, 641–654.
64 J. C. Dyre, P. Maass, B. Roling and D. L. Sidebottom, *Rep. Prog. Phys.*, 2009, **72**, 046501.
65 C. Gainaru, E. W. Stacy, V. Bocharova, M. Gobet, A. P. Holt, T. Saito, S. Greenbaum and A. P. Sokolov, *J. Phys. Chem. B*, 2016, **120**, 11074–11083.
66 G. P. Johari and E. Whalley, *J. Chem. Phys.*, 1981, **75**, 1333–1340.
67 H. Montes, K. Mazeau and J. Y. Cavaille, *Macromolecules*, 1997, **30**, 6977–6984.
68 J. Heijboer, *Proceedings of the International Conference on the Physics of Non-crystalline Solids*, 1965, p. 231.
69 J. Heijboer, J. M. A. Baas, B. Van der Graaf and M. A. Hoefnagel, *Polymer*, 1987, **28**, 509.
70 K. D. Kreuer, *Solid State Ionics*, 2000, **136–137**, 149–160.
71 A. B. Mostert, *J. Mater. Chem. B*, 2022, **10**, 7108.
72 I. Popov, Z. Zhu, A. R. Young-Gonzales, R. L. Sacci, E. Mamontov, C. Gainaru, S. J. Paddison and A. P. Sokolov, *Commun. Chem.*, 2023, **6**, 77.
73 K. D. Kreuer, *Chem. Mater.*, 1996, **8**, 610–641.